Atomic Layer Deposition of Metastable β-Fe2O3 via Isomorphic Epitaxy for Photo-assisted Water Oxidation

Journal:	*ACS Applied Materials & Interfaces*
Manuscript ID:	am-2014-07065y
Manuscript Type:	Letter
Date Submitted by the Author:	13-Oct-2014
Complete List of Authors:	Emery, Jonathan; Argonne National Laboratory, Materials Science Division Schleputz, Christian; Argonne National Laboratory, X-ray Science Division Guo, Peijun; Northwestern University, Materials Science and Engineering Riha, Shannon; Argonne National Laboratory, Materials Science Division Chang, Robert; Northwestern University, Materials Science and Engineering Martinson, Alex; Argonne National Laboratory, Materials Science Division

Atomic Layer Deposition of Metastable β-Fe_2O_3 via Isomorphic Epitaxy for Photo-assisted Water Oxidation

Jonathan D. Emery[†], Christian M. Schlepütz[‡], Peijun Guo[§], Shannon C. Riha[†], Robert P. H. Chang[§], Alex B. F. Martinson[†,*]

[†]Materials Science Division, Argonne National Laboratory, 9700 S. Cass Ave., Argonne, Illinois 60439, USA
[‡]X-ray Science Division, Argonne National Laboratory, 9700 S. Cass Ave., Argonne, Illinois 60439, USA
[§]Department of Materials Science and Engineering, Northwestern University, 2220 Campus Drive, Evanston, Illinois 60208, USA

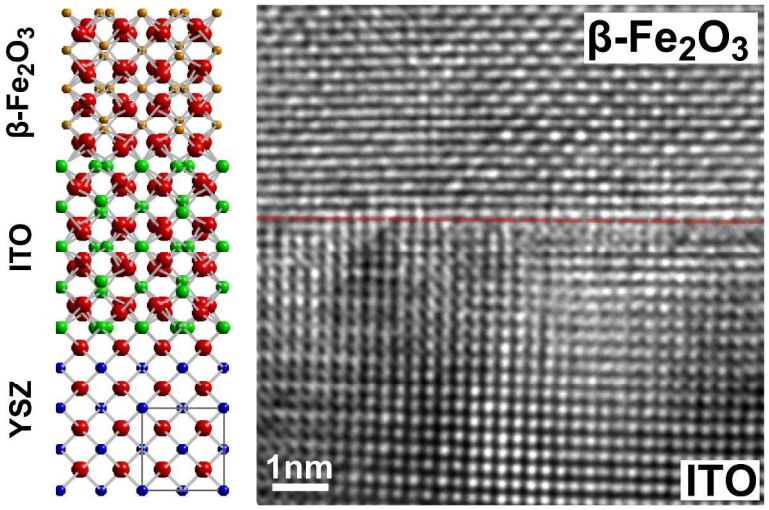

Abstract

We report the growth and photoelectrochemical (PEC) characterization of an uncommon bixbyite phase of iron(III) oxide (β-Fe_2O_3) epitaxially stabilized via atomic layer deposition on an conductive, transparent, and isomorphic template (Sn-doped In_2O_3). As a photoanode, unoptimized β-Fe_2O_3 ultrathin films perform similarly to their ubiquitous α-phase (hematite) counterpart, but reveal a more ideal bandgap (1.8 eV), a ~0.1 V improved photocurrent onset potential, and longer wavelength (>600 nm) spectral response. Stable operation under basic water oxidation justifies further exploration of this atypical phase and motivates the investigation of other unexplored metastable phases as new PEC materials.

Keywords: atomic layer deposition, iron(III) oxide, α-Fe_2O_3, β-Fe_2O_3, PEC water oxidation, epitaxial stabilization

Main Text

Semiconducting thin films suitable for large-scale solar energy conversion applications are limited to a class of materials that are non-toxic, inexpensive, easily processable, and earth abundant. It is, however, possible to broaden or improve the properties of this narrow class of materials through synthesis and utilization of uncommon, metastable phases. Such stabilized phases can be selected via judicious tuning of, for example, growth conditions, substrate selection, morphology, or post-processing. Epitaxial phase stabilization is one route to select a non-equilibrium phase over an equilibrium phase (see reviews [1-3] and references therein). The energetic benefits gained from the formation of a (semi-) coherent, lattice-matched interface during epitaxial growth not only allows for selection of metastable crystalline phases, but also provides an opportunity to improve thin film crystalline quality through larger grain size, more uniform nucleation, and creation of low defect density crystallites and interfaces [2]. This stabilization technique has not only enabled fundamental studies of many rare phases, but in some cases has yielded materials possessing improved properties and new functionality in, for example, fields such as multiferroics [4], non-linear optics [5], and high-temperature superconductors [6].

Atomic layer deposition (ALD) has become one of the most versatile routes to producing high-quality metal oxides, sulfides, nitrides, and many pure metals [7-9]. ALD is a sequential, self-limiting growth technique that is, by nature, well-suited to conformal, large-area coating of high aspect ratio frameworks with sub-nanometer digital thickness control. Although not typical, a small subset of ALD processes has been observed to produce epitaxial thin films by utilizing a suitable substrate (see Ref [9], and references therein). In this Letter, we report two technologically relevant additions to this epitaxial ALD subset which utilize cubic yttria-stabilized zirconia (YSZ) as the single crystal support. First, we briefly report the epitaxial ALD of Sn-doped In_2O_3 (ITO) on YSZ. Then, we use this epitaxial ITO/YSZ as an isomorphic growth template for the stabilization of the metastable bixbyite phase of iron (III) oxide (β-Fe_2O_3), enabling a scalable, low-temperature (~200° C), and highly controlled production method for β-Fe_2O_3. The uncommon β phase is assessed as a photoanode for the photo-assisted oxidation of water and is found to behave comparably to the commonly studied α-Fe_2O_3 (hematite), but is able to harvest a larger range of the visible spectrum and exhibits a more favorable onset potential as observed in the presence of an efficient hole scavenger.

There are a limited number of earth-abundant materials known to satisfy the demands required of the photoabsorber for practical photoelectrochemical (PEC) water oxidation [10-13]. Some of the most successful are visible-gap semiconductors, which must generate holes with sufficient potential to oxidize water, and with lifetimes long enough to overcome the sluggish kinetics of the oxygen evolution reaction (OER). The corrosive aqueous operating conditions further reduces the list of viable candidates expected to endure this environment to only a handful of the most robust materials, most of which are oxides. To date, hematite is one of the most promising

of these anode materials [14,15]. α-Fe_2O_3 is a stable phase of iron(III) oxide and exhibits a corundum structure (space group $R\bar{3}c$) with a 1.9-2.2 eV bandgap and valance band sufficiently positive to oxidize water. Within the last 10 years, improvements in control of morphology, doping, and surface chemistry of α-Fe_2O_3 photoanodes have spurred a series of improved solar-to-hydrogen efficiencies [14], with record PEC water oxidation photocurrent presently at 4.32 mA/cm^2 at 1.23 V vs the reversible hydrogen electrode (RHE), providing a net solar-to-current efficiency of ~0.6% [16].

Photoelectrochemical (PEC) investigations of non-hematite iron oxide binary phases, including $Fe_{1-x}O$, β-Fe_2O_3, γ-Fe_2O_3, ε-Fe_2O_3, and Fe_3O_4, are scarce. This is due to various deficiencies including a very small bandgap (Fe_3O_4 [0.1 eV]), degenerate doping ($Fe_{1-x}O$ and Fe_3O_4), or challenges associated with synthesis as electrodes (β-Fe_2O_3 and ε-Fe_2O_3). The β-Fe_2O_3 polymorph, which is our focus here, has no reported natural occurrence, and possesses a bixbyite-type crystal structure (space group $Ia\bar{3}$) with lattice parameter a = 9.40 [17]. It has been synthesized in nanoparticulate form via hydrolysis of $FeCl_3$ [17], solid-state reaction with NaCl and $Fe_2(SO_4)_3$ [18,19], and thermal decomposition of either $Fe(C_{10}H_9CHO)$ or $FeSO_4$ in mesoporous SiO_2 [20]. Thin films of varying purity have also been fabricated using chemical vapor deposition [21-24]. Researchers are now exploring the application of β-Fe_2O_3 for pigments [25], sensing [26,27], and photo-reformation of renewable oxygenates [28].

β-Fe_2O_3 is thermodynamically unstable, with reports of transformation to either α-Fe_2O_3 or γ-Fe_2O_3 at temperatures greater than ~500°C, depending on the β-Fe_2O_3 morphology and annealing conditions [29]. While pure hematite is a canted antiferromagnet or weak ferromagnet at room temperature, β-Fe_2O_3 is paramagnetic at room temperature. In addition, β-Fe_2O_3 is reported to possess a bandgap as low as 1.7 eV [21], suggesting the possibility that it could provide superior solar absorption as compared to α-Fe_2O_3 and therefore make it a more suitable OER photoanode. This smaller bandgap would also make β-Fe_2O_3 an outstanding candidate for use in tandem photoelectrochemical cells, for which recent modeling studies predict that an optimized system will require precisely a 1.7 eV bandgap top cell [30,31]. Despite these promising signs, β phase iron oxide has not previously been considered for PEC water splitting applications due to its synthetic elusivity. We do note, however, that the β phase may have more influence in the study of iron oxide photoanodes than previously thought. For example, Liang *et al*. have shown that Si-doping of Fe_2O_3 during spray pyrolysis can have the unintended consequence of partial β-Fe_2O_3 stabilization, which can be further influenced by choice of substrate [32]. Therefore, considering the current trends of employing dopants (see Ref. [33] and references therein) and substrate-film interfacial layers [34-38] to improve PEC performance of iron oxide films, a clear understanding of the often unintended consequences (including non-equilibrium phase stabilization) of these treatments is necessary to understand the resultant PEC behavior. Before considering these implications, however, β-Fe_2O_3 deserves a thorough investigation as a PEC water-splitting material in its own right.

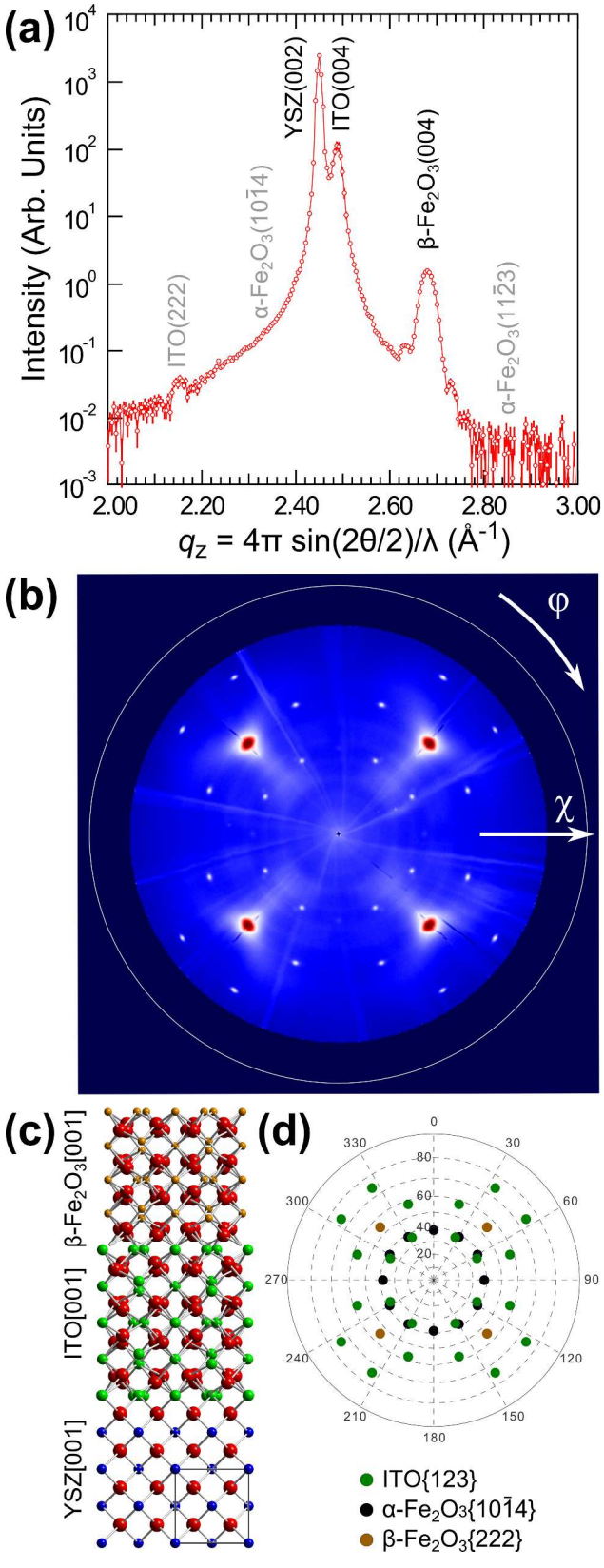

In order to access the photoelectrochemical properties of β-Fe_2O_3 we sought a substrate template that is conductive, transparent, and lattice-matched. First, low-index [(001)-, (011)-, and (111)-oriented], double-side polished single crystal YSZ substrates were annealed for 3 hours in flowing O_2 at 1100°C to remove polishing damage and achieve atomically flat surfaces. Next, a ~40 nm thick tin-doped indium oxide (ITO) film was grown by ALD at 225 °C on the YSZ substrates (following the procedures of Ref. [39]) to provide a epitaxial (see Fig. S1), transparent and conducting underlayer template. Heteroepitaxial growth of ITO(001) on YSZ(001) is readily achieved due the small lattice mismatch (-1%) between YSZ and ITO (0.512 vs 1.012 nm) and similar oxygen sublattices [40]. Finally, a ~20 nm thick Fe_2O_3 film was deposited using ferrocene [$Fe(Cp)_2$] and ozone (O_3) at 200 °C according to the ALD procedure established in Ref [41]. A complete description of all growth parameters is included in the Methods section in the Supplementary Information (SI). To our knowledge, there is no literature precedence for the epitaxial growth of β-Fe_2O_3 on any substrate using any deposition technique. However, epitaxial growth is often observed between isomorphic systems with similar material chemistries, even at large (>3%)

Figure 1: X-ray characterization of β-Fe_2O_3 grown on ITO(001)‖YSZ(001). (a) Out-of-plane thin-film X-ray diffraction. Apart from a weak polycrystalline ITO(111) signal, only the reflections from YSZ(002), ITO(004), and β-Fe_2O_3(004) are present, indicating cube-on-cube-on-cube epitaxy. Unobserved α-Fe_2O_3 reflections that would appear within this $|q|$ range are denoted in gray. (b) X-ray pole figure acquired over a $|q|$ range of 2.25-2.35 $Å^{-1}$ encompassing ITO{123}, β-Fe_2O_3{222}, and α-Fe_2O_3{10$\underline{1}$4} families of reflections. Intensity is logarithmically scaled. (c) An idealized cube-on-cube-on-cube heteroepitaxial oxide stack produces simulated pole figures in (d) which match well with the measured data in (b).

lattice mistmatch [2]. ITO provides an isomorphic substrate with 7% lattice mismatch for growth of β-Fe_2O_3.

To assess the phase and orientation of ALD-grown Fe_2O_3 films on ITO/YSZ, we performed conventional θ-2θ scans and X-ray pole figure measurements. Data for the Fe_2O_3 grown on ITO(001)||YSZ(001) is shown in Figure 1, while data for Fe_2O_3 on ITO(011)||YSZ(011) and Fe_2O_3 on ITO(111)||YSZ(111) is provided in Figure S2 in the SI. Figure 1(a) shows specular thin film diffraction data as a function of out-of-plane momentum transfer, $q_z = 4\pi \sin(2\theta/2)/\lambda$, where 2θ is the scattering angle and λ = 0.752 Å is the X-ray wavelength. The strong peaks are indexed as YSZ(002), ITO(004), and β-Fe_2O_3(004), respectively, as a function of increasing q_z. Kiessig fringes resolved about the β-Fe_2O_3(004) reflection attest to the uniformity, smoothness, and well-defined thickness of the β-Fe_2O_3 film. We note that there is a weak [$1/10^4$ as intense as the ITO(004) reflection] ITO(222) peak at q_z = 2.16 arising from a small minority of misoriented ITO crystallites.

X-ray pole figures for β-Fe_2O_3 grown on ITO(001)||YSZ(001) in Figure 1(b) [data for other orientations are provided in the SI, Figure S2] are representations of the statistical distribution of the crystallite orientations within a sample, plotted as a function of colatitude angle χ and azimuthal angle φ. The use of synchrotron radiation at the Advanced Photon Source's Sector 33-BM-C and an area detector enabled the simultaneous collection of reflections satisfying Bragg conditions in the $|q|$ range of = 2.25-2.35 $Å^{-1}$ (*e.g.* Refs. [42,43]). This range encompasses only the ITO{123}, β-Fe_2O_3{222}, and α-Fe_2O_3{10$\underline{1}$4} family of reflections. Comparison of the data in Figure 1(b) with simulated patterns [Figure 1(d)], derived from a cube-on-cube-on-cube epitaxial relationship [Figure 1(c)], show excellent agreement, thereby validating the epitaxial model. We note that the pole figure data in Figure 1(b) does show exceedingly weak Bragg reflections from <1% phase fraction of epitaxial α-Fe_2O_3 [compare Figs. 1(b) and 1(d)]. A brief discussion of this trace phase is included in the SI. Despite the high phase sensitivity of the synchrotron-based measurement, no intensity from α-Fe_2O_3{10$\underline{1}$4} reflections were observable for the other low-index systems (Fig. S2), indicating crystalline-phase pure films. Supplementary phase verification from Raman scattering is also provided as Fig. S3. Hereafter, we will refer to these epitaxial β phase films by their out-of-plane orientation, *e.g.* β-Fe_2O_3(001)||ITO(001)||YSZ(001) is simply β-Fe_2O_3(001).

High-resolution cross-sectional transmission electron microscopy (TEM) of the β-Fe_2O_3(001)||ITO(001) boundary provides further insight into the coherency and quality of the heterointerface. Figure 2 shows the TEM image of the β-Fe_2O_3(001)||ITO(001) interface and the electron diffraction patterns of β-Fe_2O_3, ITO, and YSZ, all along the [100] direction. The Fe_2O_3(001)||ITO(001) cube-on-cube epitaxy is clearly revealed in Figure 2(a), and the crystallinity of the β-Fe_2O_3 is confirmed by the nano-beam diffraction [Figure 2(b)]. The diffraction also indicates that the epitaxy is preserved throughout the entire β-Fe_2O_3 sample thickness. Interfacial strain due to the large lattice mismatch between β-Fe_2O_3 and ITO (~7%) is mitigated via the formation of misfit dislocations in β-Fe_2O_3 (Fig. S4).

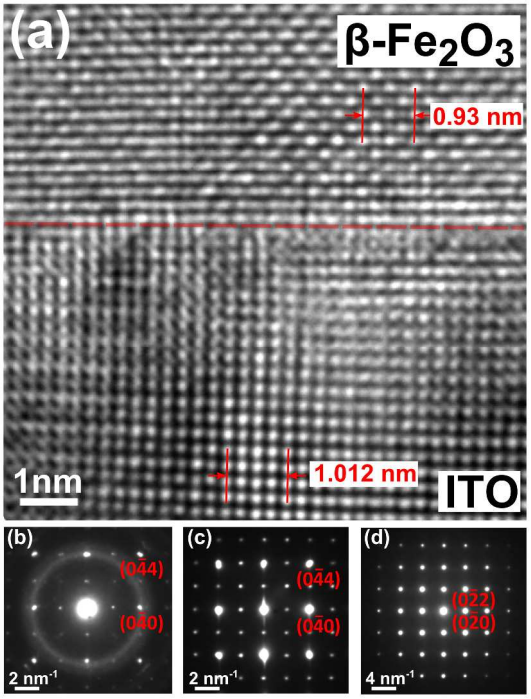

Figure 2: High-resolution cross-sectional TEM results. (a) TEM image showing the β-Fe_2O_3(001)||ITO(001) interface. (b)-(d) Electron diffraction patterns along the [100] axes of β-Fe_2O_3, ITO, and YSZ, respectively. The rings in (b) are due to the amorphous platinum layers on top of the β-Fe_2O_3 layer.

With a clear understanding of the structure and phase of these Fe_2O_3 films, we proceed to optical and PEC characterization. Figure 3(a) shows reflectance-corrected absorbance spectra for all low-index orientations of β-Fe_2O_3, as well as comparative data for α-Fe_2O_3 on fluorine-doped tin oxide (FTO) and polycrystalline β-Fe_2O_3/ITO on fused quartz (FQ). For β-Fe_2O_3/ITO/FQ phase verification, see Raman data in Fig. S3. There is little difference in the absorbance between the three orientations of epitaxial β-Fe_2O_3, but the β-Fe_2O_3/ITO/FQ shows comparatively weaker absorption at shorter wavelengths. This may be attributable to thickness variation between epitaxial and polycrystalline β-Fe_2O_3, but previous report have found reduced absorption in α-Fe_2O_3 to be correlated with decreased crystallite size and Fe-O_6 octahedral distortion [44]. Compared to α phase samples, the β phase samples lack distinct optical absorption features. Literature reports of absorption spectra for β-Fe_2O_3 agree closely with our observations in Figure 3(a) [21,22]. However the presence of some amorphous phase fraction is not inconsistent with the optical properties, nor can it be excluded by the diffraction or Raman data.

Tauc plots [$\alpha h\upsilon^n$ *vs* hυ, where α is the absorption coefficient and hυ is the photon energy] assuming an indirect allowed transition (n = 1/2) [22] reveal a bandgap of 1.8 eV for all β phase thin films [Figure 3(b)]. This value is 0.1 eV less than our α-Fe_2O_3 control sample and as much as 0.4 eV smaller than the commonly cited α-Fe_2O_3 bandgap. If photoresponsive, the smaller

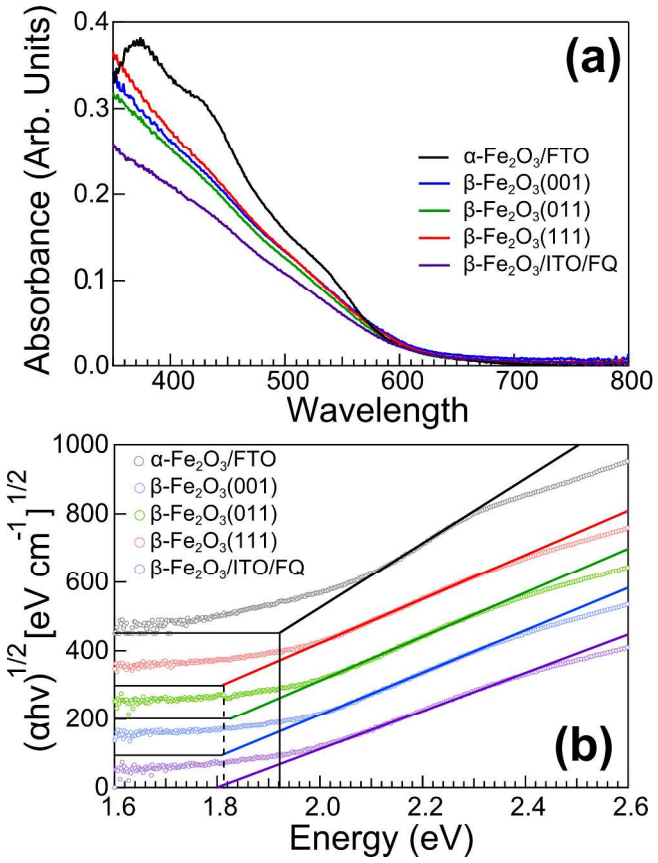

Figure 3. Optical absorbance data for β-Fe_2O_3 series and α-Fe_2O_3 control. (a) Reflection-corrected absorbance for epitaxial β phase thin films are nominally identical, while polycrystalline β-Fe_2O_3/ITO/FQ shows weaker absorption and the α-Fe_2O_3 control shows more distinct optical transitions. (b) Allowed, indirect bandgap Tauc analysis estimates a consistently lower bandgap for all β phase thin films as compared to the α phase. Tauc plots are offset for clarity.

bandgap of β-Fe_2O_3 may ultimately prove to be an advantage over α-Fe_2O_3 for application in tandem PEC water splitting cells as predicted by recent bandgap optimization models [30,31].

PEC behavior for the β-Fe_2O_3 series was assessed by measuring current density (J) as a function of applied voltage (V) in the dark and under AM 1.5 illumination (100 mW cm^{-2}) with a three-electrode setup in 1 M KOH. Results for post-annealed α-Fe_2O_3/FTO are included for comparison [Figure 4(a)]. Upon illumination, the epitaxial β-Fe_2O_3 samples are photoactive without post-annealing, which is atypical of Fe_2O_3 films grown by the $Fe(Cp)_2$-O_3 ALD process [45]. Photocurrent onset potentials (E_{onset}) differed between the three orientations, shifting cathodically by 0.1 V_{RHE} for β-Fe_2O_3(001) as compared to both β-Fe_2O_3(011) and β-Fe_2O_3(111). These shifts suggest the possibility of a variation in the OER reactivity of the three films due to the differing preferred orientation of the β-Fe_2O_3 crystallites. These differing preferred orientations may lead to the exposure of different crystal terminations at the semiconductor-electrolyte interface, each with distinct OER activity. Still, the plateau current for all three epitaxial samples is similar at $J \sim 0.3$ mA/cm^2. Chronoamperometry reveals that the plateau

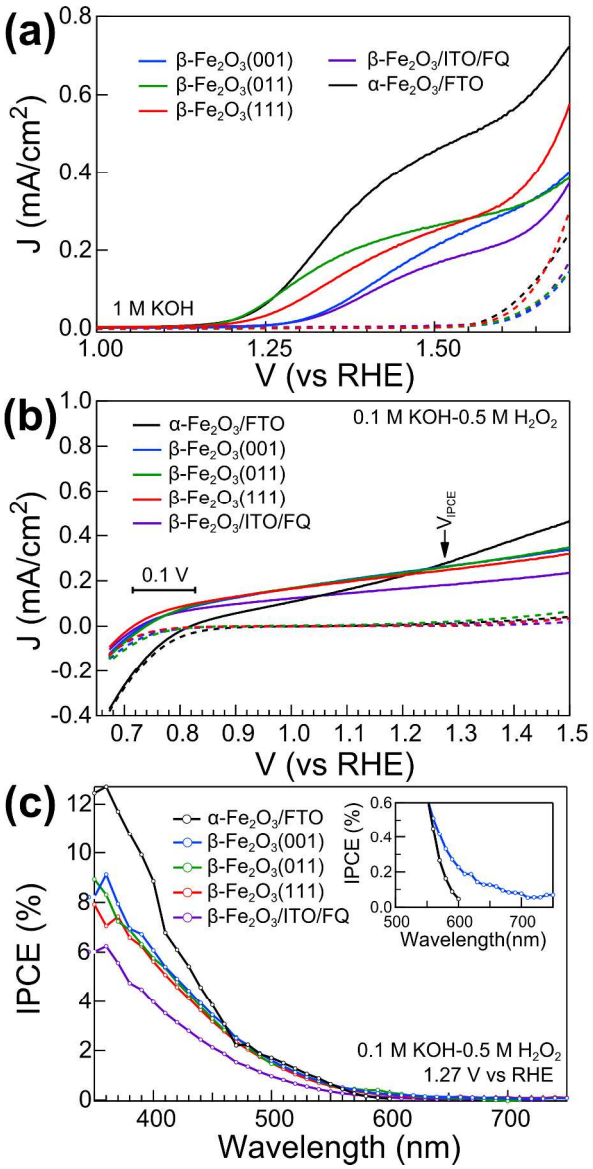

Figure 4. Photoelectrochemical data for low-index β-Fe_2O_3/ITO/YSZ, β-Fe_2O_3/ITO/FQ, and α-Fe_2O_3 photoanodes. (a) *J-V* measurements in dark (dotted line) and under white light (solid line) in 1 M KOH show photoactive as-deposited β-Fe_2O_3 films with onset voltages and plateau photocurrent dependent on crystallite orientation. (b) *J-V* measurements in dark (dotted line) and in light (solid line) in 0.1 M KOH and 0.5 M H_2O_2 reveal a 0.1 V earlier photocurrent onset for β-Fe_2O_3 relative to α-Fe_2O_3. (c) IPCEs for epitaxial β-Fe_2O_3 films measured at 1.27 vs RHE in 0.1 M KOH and 0.5 M H_2O_2 are insensitive to thin film orientation and show mildly improved IPCE above 600 nm, as compared to α-Fe_2O_3 (inset).

photocurrent is stable at 1.53 V *vs* RHE for all films for at least 1000 s (Figure S5). We also observe that single crystal YSZ substrates are not required to achieve PEC-active β-Fe_2O_3 thin films as deposition of Fe_2O_3 on polycrystalline ITO on fused quartz also results in an as-deposited photoactive β-Fe_2O_3 film. This sample was the worst performer of the β-phase series,

however, conceivably due a higher density of charge recombination centers that may be found at high-angle grain boundaries in such polycrystalline films [46].

Further disentanglement of the differences in PEC behavior among the β phase series is possible through utilization of a PEC hole scavenger [47,48]. Use of H_2O_2 as a hole scavenger circumvents hole capture limitations when assessed in conjunction with *J-V* measurements employed in conventional KOH electrolyte [48]. We therefore performed *J-V* measurements in 0.1 M KOH and 0.5 M H_2O_2 for both the β phase series and the α phase control [Figure 4(b)]. In contrast to the results in Figure 4(a), all epitaxial β-Fe_2O_3 samples exhibited essentially identical *J-V* behavior, implying the differences observed without H_2O_2 are dominated by changes in water oxidation (OER) catalytic efficiency at the β-Fe_2O_3/electrolyte interface. In addition, the β-Fe_2O_3/ITO/FQ sample, while exhibiting a similar onset potential to epitaxial β-phase samples, still shows a lower plateau current density. The lower light harvesting efficiency of this polycrystalline film will contribute to lower performance but is not sufficient to fully account for the difference. This further corroborates the possibility that the lower performance of the polycrystalline β-Fe_2O_3 may be related to its grain structure and resulting bulk recombination states at β-Fe_2O_3 grain boundaries and/or the ITO/β-Fe_2O_3 interface.

The utilization of the hole scavenger also allows for the OER-independent comparison of α- and β-Fe_2O_3 PEC performance. In general, the high overpotentials required to activate α-Fe_2O_3 photoanodes in water are attributed to electron-hole recombination losses in the bulk, depletion, and surface regions of the film. However, as observed by Dotan *et al*., [48] the elimination of the hole injection barrier isolates bulk and depletion region contributions in the *J-V* data. In the presence of H_2O_2, we find a consistently more cathodic onset potential in all β samples by ~0.1 V_{RHE} as compared to the α phase control. This suggests that the β-Fe_2O_3 either exhibits a significantly lower recombination rate or possesses a negatively shifted flat-band potential relative to α-Fe_2O_3, thereby reducing the applied potential required for the separation of charge carriers. While the development of a larger built-in photovoltage has not been excluded, it seems less likely given a smaller bandgap and comparable photon-to-current efficiency (see discussion below). As such, the band alignment of β-Fe_2O_3 may be inherently better suited to PEC water oxidation relative to α-Fe_2O_3. However, we note that cathodic shifts in the onset potential have also been achieved in α-Fe_2O_3 photoanodes through by utilizing oxide buffer layers prior to Fe_2O_3 deposition [36] or electron blocking layers that selectively pass holes to the electrolyte. Regardless, as significant modification of inherent materials properties (bulk recombination rate, band edge alignment) is rare, phase selection strategies such as β-phase stabilization provide an uncommon opportunity to circumvent these limits. While utilization of a hole scavenger in practical applications is unrealistic, the lower onset potential for β-Fe_2O_3 photocurrent in H_2O_2 solutions suggests ample room for future improvements by using OER surface catalysts - a route to reducing hole injection barrier without sacrificial reagents.

Incident photon-to-current efficiencies (IPCEs), Figure 4(c), were acquired at 1.27 V *vs* RHE in 0.1 M KOH and 0.5 M H_2O_2 to minimize the influence of OER surface reaction kinetics and to probe IPCE behavior at comparable current densities. Epitaxial β-Fe_2O_3 films behave nearly identically. As is consistent with the generally lower photocurrent for polycrystalline β-Fe_2O_3 at all applied potentials in the *J-V* measurements [Figure 4(a)-(b)], the β-Fe_2O_3/ITO/FQ heterostructures shows consistently lower IPCE across the entire spectrum. All β phase samples have slightly lower IPCEs compared to the α phase in the blue until ~460 nm, at which point (inset) the two phases are indistinguishable before a drop-off in α phase IPCE at 550 nm. α-Fe_2O_3 IPCE data is at the dark current floor beyond 600 nm, while the β-Fe_2O_3 samples (Figure 4(c) inset shows only β-Fe_2O_3(001) for clarity) have weak, but measureable (0.1%), IPCE in this regime. Although the IPCE of these unoptimized β phase samples above 600 nm is quite low, the extension of photosensitivity into the red part of the solar spectrum is clearly a real advantage of this phase. Stable photocurrent densities recorded under pH 13.1 operation for at least 15 minutes (Fig. S5) further attest to the potential of β-Fe_2O_3 in water oxidation applications.

While there is little work on the influence of epitaxy on Fe_2O_3 photoanodes for PEC water splitting (for examples, see Ref. [49-51]), those works are tangential to the recent trend in the utilization of oxide underlayers to improve α-Fe_2O_3 PEC performance. The insights reported herein provide improved understanding of the mechanism by which underlayers influence α-Fe_2O_3 water oxidation behavior, including crystallographic templating effects or minority phase contributions. We first cite Zandi *et al*., who found enhanced PEC behavior for annealed, ultrathin (< 18 nm) α-Fe_2O_3 films on commercial ITO [38]. Due to the similarity between their substrate selection and ours, it is possible that they also stabilized β-Fe_2O_3 during growth and transformed it to α-Fe_2O_3 upon annealing at 500 °C (no as-deposited data were presented). The morphology of the β-Fe_2O_3 may dictate the properties of the resultant α-Fe_2O_3 film and should be more clearly understood to precisely control its properties. The mechanism for the improved structure afforded by other underlayers is less clear due to their X-ray amorphous nature (for tabulated crystallinity results, see Ref. [9]) at the reported deposition conditions. Still, short and medium range order surface atom ordering may significantly influence the crystallinity of the subsequently grown thin films. ALD of Nb_2O_5 using $Nb_2(OC_2H_5)_{10}$ and H_2O is nominally amorphous throughout the ALD window. Growth of TiO_2 at 120 °C using tetrakis(dimethylamino)Ti(IV) and water, as reported in Ref. [37], is also amorphous, as well as WO_3 using $W_2(NMe_2)_6$ and H_2O. ALD of Ga_2O_3 under the quoted growth conditions and annealing conditions of Ref. [36] was also found to be amorphous [52]. Even if crystallization does occur, a stable monoclinic β-Ga_2O_3 phase, not corundum-type α-Ga_2O_3 is expected to develop at ~700 °C. This does not preclude improved crystallinity of α-Fe_2O_3 when deposited on a Ga_2O_3 buffer layer, and indeed subsequent analyses revealed sharper and more intense α-Fe_2O_3 Raman features for similar samples [38] as is consistent with formation of large, homogenous crystalline grains. Regardless, any designation of improved crystallinity due to isostructural

templating is unlikely in this case as well, and care must be taken when identifying such mechanisms as the source for improved PEC performance.

In conclusion, we have reported the epitaxial stabilization of the uncommon β phase of Fe_2O_3 using ALD and an isomorphic ITO/YSZ substrate. This isomorphic stabilization also occurs for polycrystalline ITO grown on fused quartz, thereby eliminating the need for a single crystal substrate to obtain the β phase. β-Fe_2O_3 films are crystalline and photoactive as deposited, properties that are atypical for ALD-grown Fe_2O_3 films using $Fe(Cp)_2$ and O_3. The orientation of β phase crystallites is controlled through selection of the epitaxial ITO/YSZ substrate, which influences PEC activity when measured in 1 M KOH, but not when employing a 0.5 M H_2O_2 as a rapid hole scavenger. This indicates that while the surface-dominated recombination and OER properties of β-Fe_2O_3 are affected by crystallite orientation, the bulk film properties are not, as may be expected for a highly symmetric crystal system. When measured in 0.5 M H_2O_2, β-Fe_2O_3 shows a 0.1 V more cathodic onset potential relative to the α phase. The β phase also shows stable operation in strong base in addition to a slightly enhanced IPCE in the red (>600 nm) portion of the solar spectrum, likely due to a bandgap that is at least 0.1 eV more narrow. The modest improvements in bandgap, photocurrent onset, and red light conversion efficiency for β-Fe_2O_3 are enhancements that are notoriously difficult to achieve in α-Fe_2O_3. As this work represents the first PEC water oxidation study of β-Fe_2O_3, further optimization and assessment will be required to fully assess the potential of this iron(III) oxide phase for PEC solar energy conversion applications.

Supporting Info

Supporting information provides X-ray diffraction data verifying ITO/YSZ epitaxy, specular X-ray scattering and pole figure measurements for β-Fe_2O_3(011) and β-Fe_2O_3(111), Raman scattering for all samples, additional TEM images, and chronoamperometry data to assess β-Fe_2O_3 stability at PEC operating conditions.

Acknowledgments:

This work was supported as part of the Argonne-Northwestern Solar Energy Research (ANSER) Center, an Energy Frontier Research Center funded by the U.S. Department of Energy, Office of Science, Office of Basic Energy Sciences, under Award Number DE-SC0001059. The authors would like to thank Dr. D. Bruce Buchholz for growth of the preliminary epitaxial ITO films by PLD. This research, including X-ray studies at the Advanced Photon Source, was performed at Argonne National Laboratory, a U.S. Department of Energy, Office of Science, Laboratory operated under Contract No. DE-AC02-06CH11357 by UChicago Argonne, LLC. We acknowledge use of beamlines 13-BM-C and 33-BM-C for acquisition of the X-ray diffraction data. SEM/FIB and TEM were performed at the EPIC facility, located in NUANCE Center at Northwestern University. NUANCE Center is supported by NSF-NSEC, NSF-MRSEC, Keck Foundation, the State of Illinois, and Northwestern University.

References

[1] R. Farrow. "The stabilization of metastable phases by epitaxy," Journal of Vacuum Science & Technology B **1**(2) 222-228 (1983).

[2] O.Y. Gorbenko, S.V. Samoilenkov, I.E. Graboy, A.R. Kaul. "Epitaxial Stabilization of Oxides in Thin Films," Chemistry of Materials **14**(10) 4026-4043 (2002).

[3] D.G. Schlom, L.Q. Chen, X. Pan, A. Schmehl, M.A. Zurbuchen. "A thin film approach to engineering functionality into oxides," Journal of the American Ceramic Society **91**(8) 2429-2454 (2008).

[4] K. Balasubramaniam, S. Havelia, P. Salvador, H. Zheng, J. Mitchell. "Epitaxial stabilization and structural properties of $REMnO_3$ (RE= Dy, Gd, Sm) compounds in a layered, hexagonal ABO_3 structure," Applied Physics Letters **91**(23) 232901-232901-232903 (2007).

[5] R.F. Xiao, L. Ng, P. Yu, G. Wong. "Preparation of crystalline beta barium borate (β-BaB_2O_4) thin films by pulsed laser deposition," Applied Physics Letters **67**(3) 305-307 (1995).

[6] A.F. Moreira dos Santos, A.K. Cheetham, W. Tian, X. Pan, Y. Jia, N.J. Murphy, J. Lettieri, D.G. Schlom. "Epitaxial growth and properties of metastable $BiMnO_3$ thin films," Applied Physics Letters **84**(1) 91-93 (2004).

[7] M. Leskelä, M. Ritala. "Atomic layer deposition (ALD): from precursors to thin film structures," Thin Solid Films **409**(1) 138-146 (2002).

[8] S.M. George. "Atomic layer deposition: an overview," Chemical Reviews **110**(1) 111-131 (2009).

[9] V. Miikkulainen, M. Leskelä, M. Ritala, R.L. Puurunen. "Crystallinity of inorganic films grown by atomic layer deposition: Overview and general trends," Journal of Applied Physics **113**(2) 021301 (2013).

[10] N.S. Lewis, D.G. Nocera. "Powering the planet: Chemical challenges in solar energy utilization," Proceedings of the National Academy of Sciences **103**(43) 15729-15735 (2006).

[11] F.E. Osterloh. "Inorganic materials as catalysts for photochemical splitting of water," Chemistry of Materials **20**(1) 35-54 (2007).

[12] M.G. Walter, E.L. Warren, J.R. McKone, S.W. Boettcher, Q. Mi, E.A. Santori, N.S. Lewis. "Solar water splitting cells," Chemical Reviews **110**(11) 6446-6473 (2010).

[13] S. Cho, J.-W. Jang, K.-H. Lee, J.S. Lee. "Research Update: Strategies for efficient photoelectrochemical water splitting using metal oxide photoanodes," APL Materials **2**(1) 010703 (2014).

[14] K. Sivula, F. Le Formal, M. Grätzel. "Solar Water Splitting: Progress Using Hematite (α-Fe_2O_3) Photoelectrodes," ChemSusChem **4**(4) 432-449 (2011).

[15] M.J. Katz, S.C. Riha, N.C. Jeong, A.B. Martinson, O.K. Farha, J.T. Hupp. "Toward solar fuels: Water splitting with sunlight and "rust"?," Coordination Chemistry Reviews **256**(21) 2521-2529 (2012).

[16] J.Y. Kim, G. Magesh, D.H. Youn, J.-W. Jang, J. Kubota, K. Domen, J.S. Lee. "Single-crystalline, wormlike hematite photoanodes for efficient solar water splitting," Scientific Reports **3** (2013).

[17] M.B. Svendsen. "Beta-Fe_2O_3- eine neue Eisen (III) oxyd-Struktur," Naturwissenschaften **45**(22) 542-542 (1958).

[18] Y. Ikeda, M. Takano, Y. Bando. "Formation Mechanism of Needle-like α-Fe_2O_3Particles Grown Along the c Axis and Characterization of Precursorily Formed β-Fe_2O_3," Bulletin of the Institute for Chemical Research, Kyoto University **64**(4) 249-258 (1986).

[19] T. Danno, D. Nakatsuka, Y. Kusano, H. Asaoka, M. Nakanishi, T. Fujii, Y. Ikeda, J. Takada. "Crystal structure of β-Fe_2O_3 and topotactic phase transformation to α-Fe_2O_3," Crystal Growth & Design **13**(2) 770-774 (2013).

[20] S. Sakurai, A. Namai, K. Hashimoto, S.-i. Ohkoshi. "First observation of phase transformation of all four Fe_2O_3 phases ($\gamma \rightarrow \varepsilon \rightarrow \beta \rightarrow \alpha$-phase)," Journal of the American Chemical Society **131**(51) 18299-18303 (2009).

[21] L. Ben-Dor, E. Fischbein, I. Felner, Z. Kalman. "β-Fe_2O_3: Preparation of Thin Films by Chemical Vapor Deposition from Organometallic Chelates and Their Characterization," Journal of The Electrochemical Society **124**(3) 451-457 (1977).

[22] D. Barreca, G. Carraro, A. Devi, E. Fois, A. Gasparotto, R. Seraglia, C. Maccato, C. Sada, G. Tabacchi, E. Tondello. "β-Fe_2O_3 nanomaterials from an iron (II) diketonate-diamine complex: a study from molecular precursor to growth process," Dalton Transactions **41**(1) 149-155 (2012).

[23] K. Kuribayashi, R. Ueyama. "Effect of the substrate on the growth of spinel iron oxide thin films by metal-organic chemical vapor deposition," Thin Solid Films **295**(1–2) 16-18 (1997).

[24] T. Maruyama, T. Kanagawa. "Electrochromic properties of iron oxide thin films prepared by chemical vapor deposition," Journal of The Electrochemical Society **143**(5) 1675-1677 (1996).

[25] R. Zboril, M. Mashlan, K. Barcova, M. Vujtek. "Thermally induced solid-state syntheses of γ-Fe_2O_3 nanoparticles and their transformation to α-Fe_2O_3 via ε-Fe_2O_3," Hyperfine Interactions **139**(1-4) 597-606 (2002).

[26] M.M. Rahman, A. Jamal, S.B. Khan, M. Faisal. "Characterization and applications of as-grown β-Fe_2O_3 nanoparticles prepared by hydrothermal method," Journal of Nanoparticle Research **13**(9) 3789-3799 (2011).

[27] G. Carraro, D. Barreca, E. Comini, A. Gasparotto, C. Maccato, C. Sada, G. Sberveglieri. "Controlled synthesis and properties of β-Fe_2O_3 nanosystems functionalized with Ag or Pt nanoparticles," CrystEngComm **14**(20) 6469-6476 (2012).

[28] G. Carraro, C. Maccato, A. Gasparotto, T. Montini, S. Turner, O.I. Lebedev, V. Gombac, G. Adami, G. Van Tendeloo, D. Barreca. "Enhanced Hydrogen Production by Photoreforming of Renewable Oxygenates Through Nanostructured Fe_2O_3 Polymorphs," Advanced Functional Materials **24**(3) 372-378 (2014).

[29] R. Zboril, M. Mashlan, D. Petridis. "Iron (III) oxides from thermal processes synthesis, structural and magnetic properties, Mössbauer spectroscopy characterization, and applications," Chemistry of Materials **14**(3) 969-982 (2002).

[30] S. Hu, C. Xiang, S. Haussener, A.D. Berger, N.S. Lewis. "An analysis of the optimal band gaps of light absorbers in integrated tandem photoelectrochemical water-splitting systems," Energy & Environmental Science **6**(10) 2984-2993 (2013).

[31] B. Seger, I.E. Castelli, P.C.K. Vesborg, K.W. Jacobsen, O. Hansen, I. Chorkendorff. "2-Photon tandem device for water splitting: comparing photocathode first versus photoanode first designs," Energy & Environmental Science **7**(8) 2397-2413 (2014).

[32] Y. Liang, R. van de Krol. "Influence of Si dopant and SnO_2 interfacial layer on the structure of the spray-deposited Fe_2O_3 films," Chemical Physics Letters **479**(1) 86-90 (2009).

[33] Z. Li, W. Luo, M. Zhang, J. Feng, Z. Zou. "Photoelectrochemical cells for solar hydrogen production: current state of promising photoelectrodes, methods to improve their properties, and outlook," Energy & Environmental Science **6**(2) 347-370 (2013).

[34] Y. Liang, C.S. Enache, R. van de Krol. "Photoelectrochemical Characterization of Sprayed α-Fe_2O_3 Thin Films: Influence of Si Doping and SnO_2 Interfacial Layer," International Journal of Photoenergy **2008** (2008).

[35] F. Le Formal, M. Graetzel, K. Sivula. "Controlling Photoactivity in Ultrathin Hematite Films for Solar Water-Splitting," Advanced Functional Materials **20**(7) 1099-1107 (2010).

[36] T. Hisatomi, J. Brillet, M. Cornuz, F. Le Formal, N. Tétreault, K. Sivula, M. Grätzel. "A Ga_2O_3 underlayer as an isomorphic template for ultrathin hematite films toward efficient photoelectrochemical water splitting," Faraday Discussions **155** 223-232 (2012).

[37] T. Hisatomi, H. Dotan, M. Stefik, K. Sivula, A. Rothschild, M. Grätzel, N. Mathews. "Enhancement in the Performance of Ultrathin Hematite Photoanode for Water Splitting by an Oxide Underlayer," Advanced Materials **24**(20) 2699-2702 (2012).

[38] O. Zandi, J.A. Beardslee, T. Hamann. "Substrate Dependent Water Splitting with Ultrathin α-Fe_2O_3 Electrodes," The Journal of Physical Chemistry C;10.1021/jp4116657 (2014).

[39] J.W. Elam, D.A. Baker, A.B. Martinson, M.J. Pellin, J.T. Hupp. "Atomic layer deposition of indium tin oxide thin films using nonhalogenated precursors," The Journal of Physical Chemistry C **112**(6) 1938-1945 (2008).

[40] F.J. Wong, S. Ramanathan. "Nonisostructural complex oxide heteroepitaxy," Journal of Vacuum Science & Technology A **32**(4) - (2014).

[41] A.B. Martinson, M.J. DeVries, J.A. Libera, S.T. Christensen, J.T. Hupp, M.J. Pellin, J.W. Elam. "Atomic layer deposition of Fe_2O_3 using ferrocene and ozone," The Journal of Physical Chemistry C **115**(10) 4333-4339 (2011).

[42] S. Gaudet, K. De Keyser, S. Lambert-Milot, J. Jordan-Sweet, C. Detavernier, C. Lavoie, P. Desjardins. "Three dimensional reciprocal space measurement by x-ray diffraction using linear and area detectors: Applications to texture and defects determination in oriented thin films and nanoprecipitates," Journal of Vacuum Science & Technology A **31**(2) 021505 (2013).

[43] C. Mocuta, M.-I. Richard, J. Fouet, S. Stanescu, A. Barbier, C. Guichet, O. Thomas, S. Hustache, A.V. Zozulya, D. Thiaudiere. "Fast pole figure acquisition using area detectors at the DiffAbs beamline-Synchrotron SOLEIL," Journal of Applied Crystallography **46**(6) 1842-1853 (2013).

[44] N. Pailhé, A. Wattiaux, M. Gaudon, A. Demourgues. "Impact of structural features on pigment properties of α-Fe_2O_3 haematite," Journal of Solid State Chemistry **181**(10) 2697-2704 (2008).

[45] B.M. Klahr, A.B. Martinson, T.W. Hamann. "Photoelectrochemical investigation of ultrathin film iron oxide solar cells prepared by atomic layer deposition," Langmuir **27**(1) 461-468 (2010).

[46] S.C. Warren, K. Voïtchovsky, H. Dotan, C.M. Leroy, M. Cornuz, F. Stellacci, C. Hébert, A. Rothschild, M. Grätzel. "Identifying champion nanostructures for solar water-splitting," Nature Materials **12**(9) 842-849 (2013).

[47] P. Iwanski, J. Curran, W. Gissler, R. Memming. "The photoelectrochemical behavior of ferric oxide in the presence of redox reagents," Journal of The Electrochemical Society **128**(10) 2128-2133 (1981).

[48] H. Dotan, K. Sivula, M. Grätzel, A. Rothschild, S.C. Warren. "Probing the photoelectrochemical properties of hematite (α-Fe_2O_3) electrodes using hydrogen peroxide as a hole scavenger," Energy & Environmental Science **4**(3) 958-964 (2011).

[49] H. Magnan, D. Stanescu, M. Rioult, E. Fonda, A. Barbier. "Enhanced photoanode properties of epitaxial Ti doped α-Fe_2O_3(0001) thin films," Applied Physics Letters **101**(13) 133908 (2012).

[50] M. Rioult, H. Magnan, D. Stanescu, A. Barbier. "Single Crystalline Hematite Films for Solar Water Splitting: Ti-Doping and Thickness Effects," The Journal of Physical Chemistry C **118**(6) 3007-3014 (2014).

[51] A.G. Joly, J.R. Williams, S.A. Chambers, G. Xiong, W.P. Hess, D.M. Laman. "Carrier dynamics in α-Fe_2O_3(0001) thin films and single crystals probed by femtosecond transient absorption and reflectivity," Journal of Applied Physics **99**(5) 053521 (2006).

[52] L. Charles IV, I. Dezelah, J. Niinistö, K. Arstila, L. Niinistö, C.H. Winter. "Atomic layer deposition of Ga_2O_3 films from a dialkylamido-based precursor," Chemistry of Materials **18**(2) 471-475 (2006).

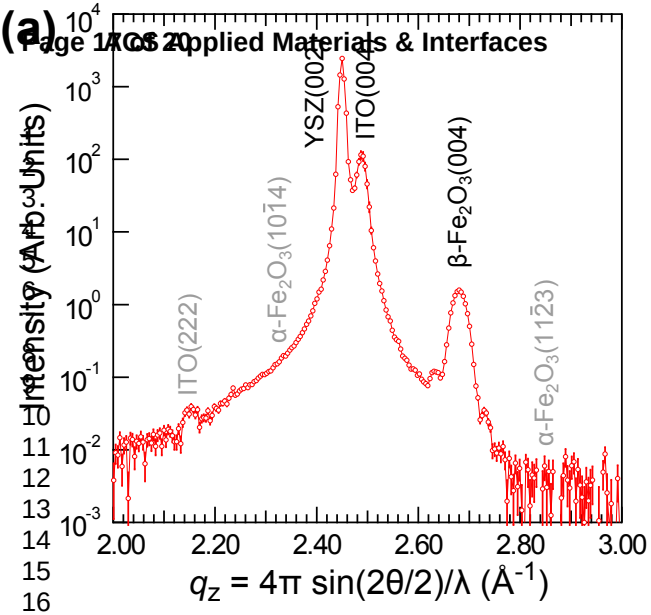

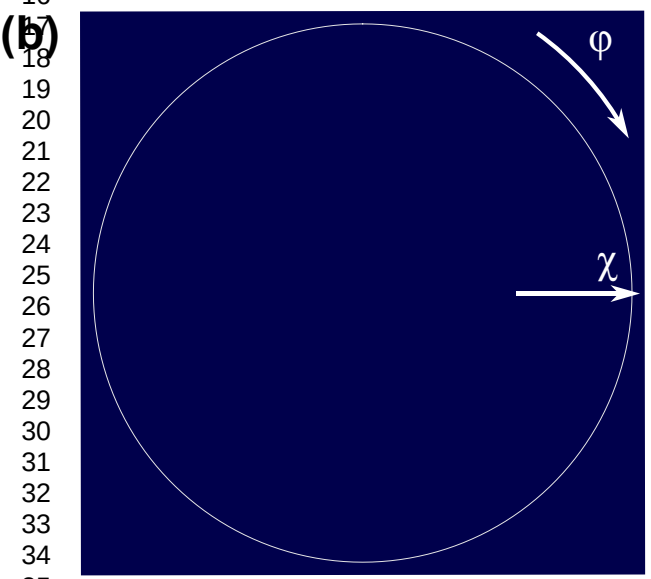

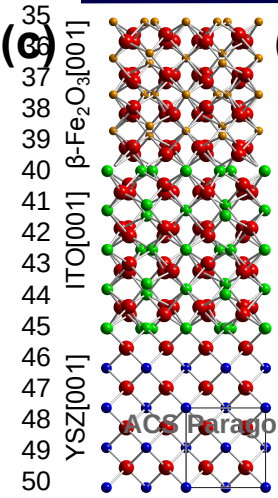

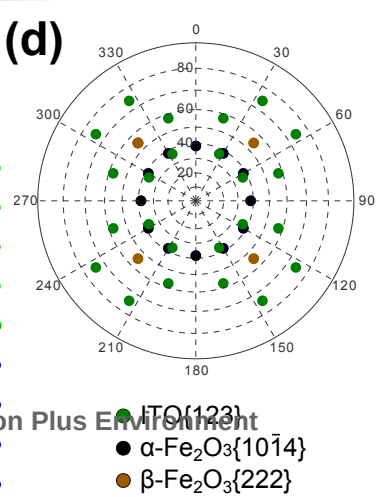

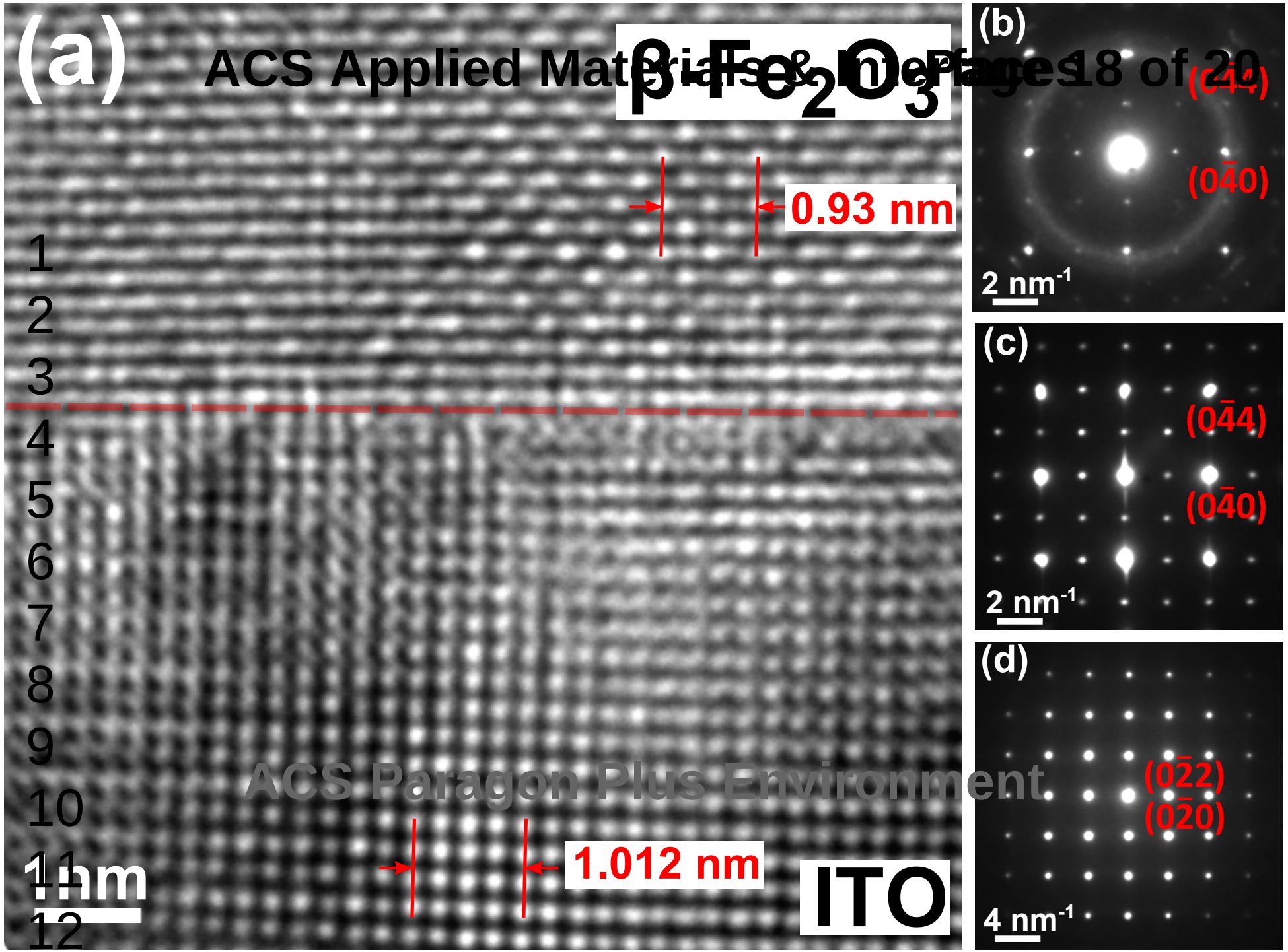
(a)
β-Fe2O3
0.93 nm
1.012 nm
ITO
ACS Paragon Plus Environment
1 nm
(b)
(04̄4)
(04̄0)
2 nm-1
(c)
(04̄4)
(04̄0)
2 nm-1
(d)
(02̄2)
(02̄0)
4 nm-1

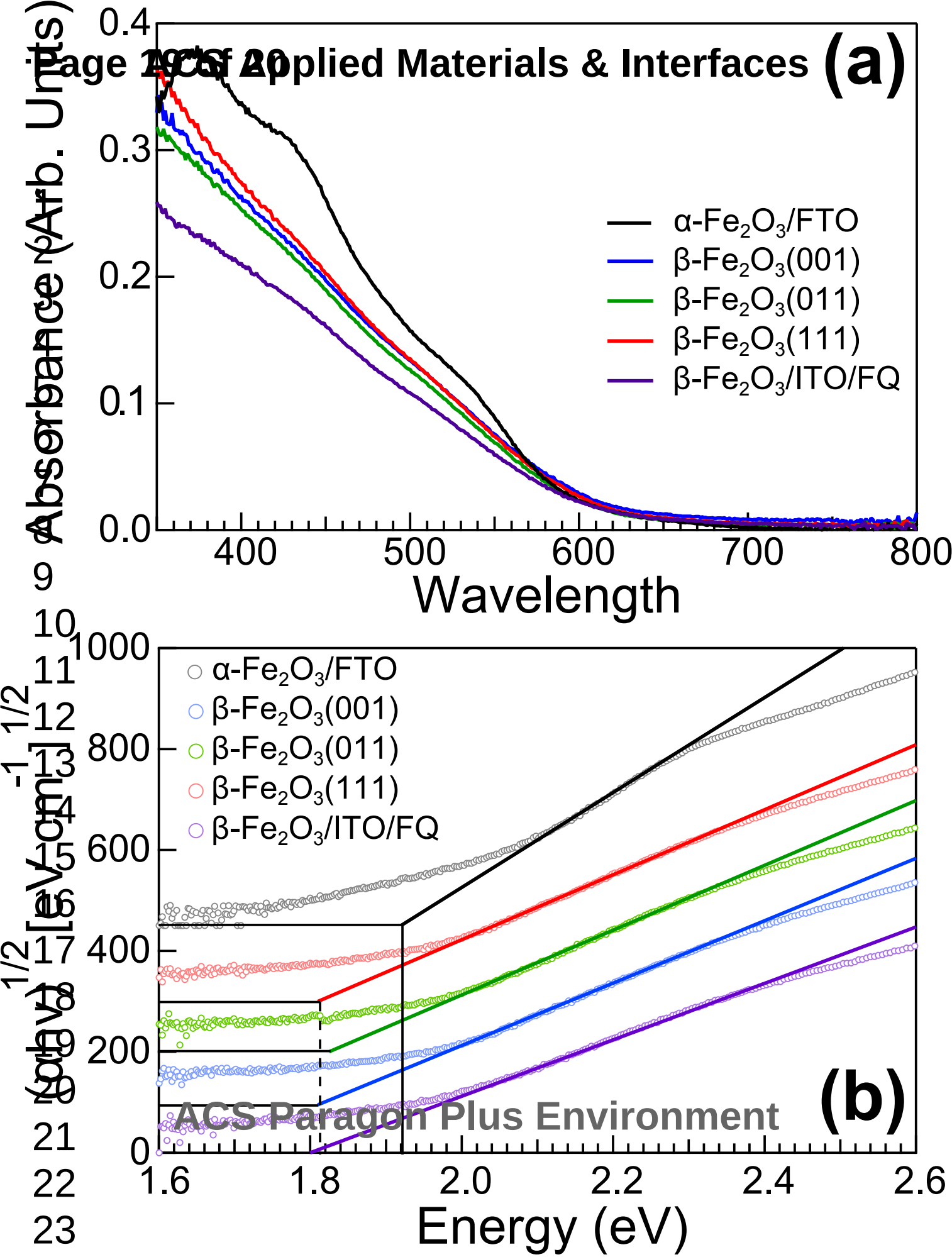
(a)
Absorbance (Arb. Units)
Wavelength
α-Fe2O3/FTO
β-Fe2O3(001)
β-Fe2O3(011)
β-Fe2O3(111)
β-Fe2O3/ITO/FQ
(b)
(αhν)^2 [eV cm^-1]^1/2
Energy (eV)
ACS Paragon Plus Environment

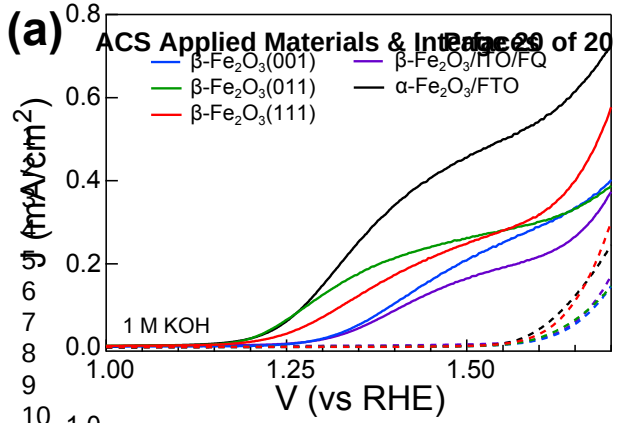
(a)
β-Fe2O3(001)
β-Fe2O3(011)
β-Fe2O3(111)
β-Fe2O3/ITO/FQ
α-Fe2O3/FTO
1 M KOH
J (mA/cm2)
V (vs RHE)

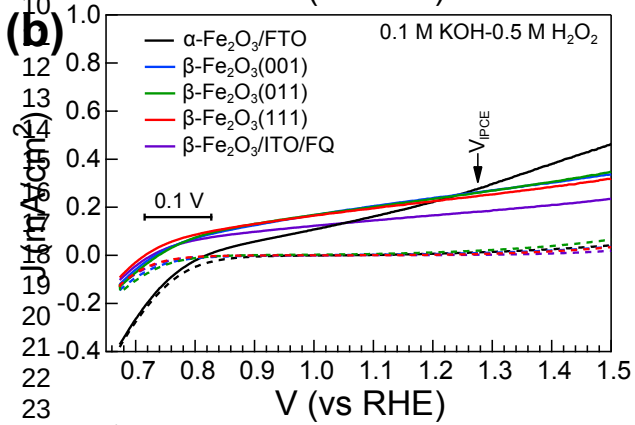
(b)
α-Fe2O3/FTO
β-Fe2O3(001)
β-Fe2O3(011)
β-Fe2O3(111)
β-Fe2O3/ITO/FQ
0.1 M KOH-0.5 M H2O2
VIPCE
0.1 V
Jphoto (mA/cm2)
V (vs RHE)

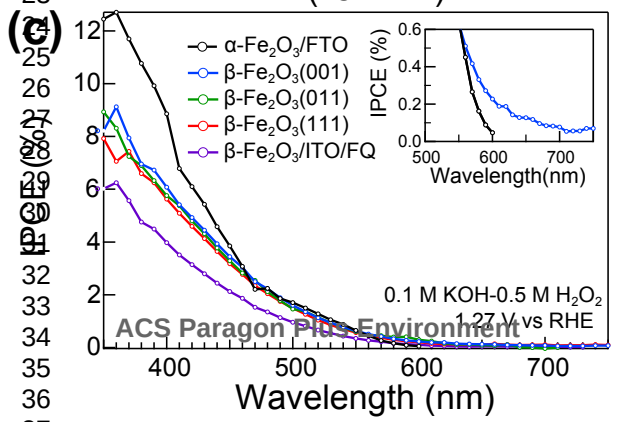
(c)
α-Fe2O3/FTO
β-Fe2O3(001)
β-Fe2O3(011)
β-Fe2O3(111)
β-Fe2O3/ITO/FQ
IPCE (%)
Wavelength(nm)
0.1 M KOH-0.5 M H2O2
1.27 V vs RHE
ACS Paragon Plus Environment
Wavelength (nm)